

## **Section 2**

Data sets, diagnostic and dynamical investigations, statistical post-processing, reanalysis, and associated studies.



# VERTICAL MACROSTRUCTURE OF FIRST- AND SECOND-ORDER TRENDS OF AIR TEMPERATURE IN THE 0–30-KM ATMOSPHERIC LAYER FROM RADIOSONDE OBSERVATIONS

O. A. Aldukhov and I. V. Chernykh

Russian Institute of Hydrometeorological Information – World Data Center, Obninsk,  
Russia, E-mail: [aoa@meteo.ru](mailto:aoa@meteo.ru), [civ@meteo.ru](mailto:civ@meteo.ru)

## Introduction

The knowledge about a vertical macrostructure of global trends of meteorological values in the atmosphere obtained from observations is necessary to study climate change. The paper presents the series of the first- and second-order trends [1] of air temperature (T) at standard heights in the 0–30-km atmospheric layer above sea level for different months, seasons and for the year as a whole. The goal of the paper and [1–5] is to show the longtime changes in the atmosphere for one period of radiosonde observations for the main aerological values.

## Data and methods

Results of observations from the CARDS global aerological dataset [6] that were updated with current data [7] for the period 1964–2018 were used in this research. The required condition for the station to be included in this study was 15-year observations from the full observation period including 2018. The Akima cubic spline interpolation method was used to calculate T values and their standard deviations ( $\sigma_T$ ) in the 0–30-km layer above sea level on the basis of standard pressure levels and specific points of vertical profiles. The linear trends were estimated for each station by using least squares method. The anomalies were computed with respect to the appropriate long-term mean values for the period 1964–2018. The statistics obtained for all stations were averaged taking into account the area of the station influence.

## Results

The Figure shows a vertical macrostructure of long-term means and standard deviations  $\sigma_T$ , the first- and second-order trends for anomalies of temperature and  $\sigma_T$  in the studied atmospheric layer for different months, seasons and the whole year.

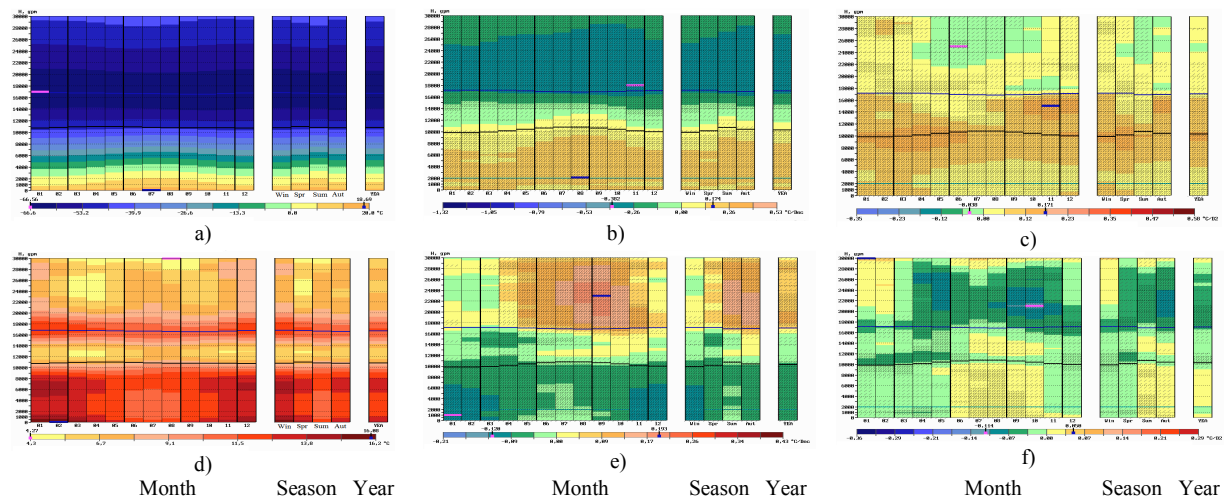


Figure. Long-term means (a, C°), first-order trends of anomalies of long-term means for T (b, C° per decade), second-order trends of anomalies of long-term means for T (c, C° per decade<sup>2</sup>), and standard deviations (d), first-order (e) and second-order (f) trends of standard deviations in the 0–30-km layer for the year as a whole, for each month and season. Winter – DJF, spring – MMA, summer – JJA, autumn – SON. Blue and pink segments correspond to maximum and minimum values. The global statistics for months and seasons were subject to twofold smoothing. The three-points smoothing was used. Trends with significance of not less than 50% are marked by the sloping line segments and those with significance of not less than 95% – by lattice. 1964–2018.

The annual changes in the long-term monthly means of temperature T in the studied layer range from -66.56 to 18.69 C°. The minimum value of the monthly means of T was detected at 17 km in January, while the maximum value was detected at 0 km in July.

The annual changes of the first-order trends of the long-term monthly means anomalies in the 0–30-km layer range from  $-0.382$  to  $0.174$  C° per decade for T. The minimum value of the first-order trends was detected at 18 km in November, while the maximum value was found at 2 km in August. Warming in the 0–10-km layer and cooling in the 14–30-km layer were determined with significance of more than 95% for all months. The most intense warming was detected mostly throughout the 1–7-km layer for all months, as well as in the entire 0–1-km layer from September to April, and at 7–9-km, from July to August. The largest cooling was detected in the 17–25-km layer for all months and additionally in the 25–26-km, 25–27-km and 25–28-km layers in spring, summer and autumn, respectively. The first order trends (positive as well as negative) were detected only in the 10–13-km layer for all months with significance of less than 95%.

The annual changes in the second-order trends of the long-term monthly means anomalies in the 0–30-km layer range from  $-0.038$  to  $0.171$  C° per decade<sup>2</sup> for temperature. Minimum and maximum values of the second-order trends were detected at 25 km in June and at 15 km in November, respectively. The second-order trends of the long-term monthly means anomalies are positive mostly in the 0–17-km layer with significance of more than 95% for all months. This implies the acceleration of warming for cases with positive values of the first-order trends, while this implies the weakening of cooling for case with negative values of the first-order trends with the year 2018 approaching. The second-order trends were detected in the 17–30-km layer with significance of more than 50% and less than 95% for all months. For T, we see both positive values for the second-order trends in 17–30-km layer for winter, spring and autumn, and negative values in the 23–30-km layer from May to August. This means the weakening of cooling in the 17–30-km layer in winter, spring and autumn and its acceleration in the 23–30-km layer from May to August with the year 2018 approaching.

The annual changes in standard deviations  $\sigma_T$  range from 4.27 to 16.08 C°. The minimum value of  $\sigma_T$  was detected at 30 km in August, while the maximum value was detected at 0 km in February. The annual changes in the first-order trends of  $\sigma_T$  range from  $-0.128$  to  $0.193$  C° per decade. The standard deviation decreases in the 0–10-km layer for all months, while in the 18–30-km layer, this increases from May to October with significance of more than 95%. The annual changes in the second-order trends of  $\sigma_T$  in the 0–30-km layer range from  $-0.114$  to  $0.050$  C° per decade<sup>2</sup>. Negative values of the second-order trends of  $\sigma_T$  at 17–28 km from April to November imply the weakening of  $\sigma_T$  increase in this layer, while positive values of the second-order trends of  $\sigma_T$  in the 0–10-km layer from June to October imply the weakening of decrease  $\sigma_T$  in this layer with the year 2018 approaching.

### Conclusions

The vertical macrostructures of the first-order and second-order linear trends of air temperature anomalies are not uniform in the 0–30 km atmospheric layer above sea level. The computations are based on global aerological datasets for the period 1964–2018. Warming at 0–10 km and cooling at 14–30 km were detected for all months. The highest acceleration in T changes was detected at 0–2 km and at 4–17 km in winter, at 0–1 km and at 4–14 km in spring, at 6–12 km in summer and at 6–17 km in autumn, at 5–16 km for the year as a whole with the year 2018 approaching. The corresponding trends were detected with significance of more than 95%.

### References

1. Aldukhov O.A., Chernykh I.V. First and second-order trends of air temperature at the surface level from global radiosonde data // Research activities in Earth system modelling. Working Group on Numerical Experimentation. Report No. 50. WCRP Report No.12/2020. Ed. E. Astakhova, July 2020, WMO, Geneva. Research Activities in Earth System Modelling (WGNE Blue Book 2020), <http://bluebook.meteoinfo.ru/>, 2020, p. 2-03-2-04
2. Aldukhov O.A., Chernykh I.V. First and second-order trends of wind speed in the 0–30 km atmospheric layer from global aerological datasets // Research activities in Earth system modelling. Working Group on Numerical Experimentation. Report No. 51. WCRP Report No. 4/2021. Ed.E.Astakhova, July 2021, WMO, Geneva, <http://bluebook.meteoinfo.ru/>, 2021 p. 2-05-2-06.
3. Aldukhov O.A., Chernykh I.V. Trends of wind speed in low troposphere from global radiosonde data// Research Activities in Atmospheric and Oceanic Modelling. WGNE Blue Book 2019, <http://bluebook.meteoinfo.ru/>, 2019, p. 2-03-2-04
4. Chernykh I.V., Aldukhov O.A. Spatiotemporal distributions of global trends of humidity and temperature in the low troposphere// Research activities in Earth system modelling. Working Group on Numerical Experimentation. Report No. 50. WCRP Report No.12/2020. Ed. E. Astakhova, July 2020, WMO, Geneva. Research Activities in Earth System Modelling (WGNE Blue Book 2020), <http://bluebook.meteoinfo.ru/>, 2020, p. 2-07-2-08
5. Aldukhov O.A., Chernykh I.V. Spatiotemporal distributions of global trends of water vapour amount in the 0–30 km atmospheric layer // Research activities in Earth system modelling. Working Group on Numerical Experimentation. Report No. 51. WCRP Report No. 4/2021. Ed.E.Astakhova, July 2021, WMO, Geneva. <http://bluebook.meteoinfo.ru/>, 2021. p. 2-03-2-04.
6. Eskridge R.E., et. al. A comprehensive aerological reference dataset (CARDS): rough and systematic errors // Bull. Amer. Meteor. Soc. 1995. **76**. 1759–1775.
7. Rudenkova T.V. Format for archiving of the current aerological data, received from GTS for PC // Proc. RIHMI-WDC, 2010, N 174, p. 41–63.

# **Intra-annual Changes of Trends of the Number of Reconstructed Cloud Layers for the Northern and Southern Hemispheres from Radiosounding Data**

I.V. Chernykh and O.A. Aldukhov

*Russian Institute of Hydrometeorological Information – World Data Center, Obninsk, Russia,*

*E-mail: [civ@meteo.ru](mailto:civ@meteo.ru), [aoa@meteo.ru](mailto:aoa@meteo.ru)*

## **Introduction**

The information about the cloud layer number is useful for studying the cloudiness vertical structure and climatic changes, and for assessing propagation conditions of electromagnetic waves. Different questions of research on the cloud layer number were discussed in [1–4]. The paper presents long-term estimates of the number ( $n$ ) of reconstructed cloud layers with the cloud amount of 0–100% of the sky surface and trends of their anomalies for the Northern and Southern Hemispheres. Calculations were conducted for the atmospheric layers of 0–2, 2–6, 6–10 and 0–10 km above the surface level. Means and trends were found for each month, season (winter – DJF, spring – MAM, summer – JJA, autumn – SON) and the year as a whole.

## **Data and methods**

To determine cloud boundaries and cloud amount [5], we used CE-method and CARDS global dataset [6] supplemented with current data [7] for the 1964–2018 period. To compute the statistics, only observations including both temperature and humidity data from the surface to the 10-km height were applied. The existence of several cloud layers with different cloud amounts was allowed. We did not consider cloud layers with thickness less than 50 m that was determined by CE-method.

## **Results**

The Table presents annual mean values and trends of anomalies of the cloud layer number with cloud amount of 0–100% of the sky surface, as well as ranges of annual variations in monthly means and trends of their anomalies for the atmospheric layers of 0–2, 2–6, 6–10, 0–10 km over the Northern and Southern Hemispheres.

The means of the cloud layer number with cloud amounts of 0–100% of the sky surface and the corresponding trends estimated for atmospheric layers of 0–2, 2–6, 6–10, 0–10 km over the Northern and Southern Hemispheres are shown in the Figure for months, seasons and the year as a whole.

The trends were estimated for each station by using the least squares method. The anomalies were calculated with respect to the corresponding long-term mean values for the period 1964–2018. The values obtained for the stations placed in the Northern and Southern Hemispheres were averaged taking into account the area of the station influence. The statistics for the Northern and Southern Hemispheres for months and seasons were subject to twofold smoothing. The three-points smoothing was used.

The results show that the means of the cloud layer number and trends of their anomalies depend on the cloud level. Their values for the middle-level cloud layers are higher than those for the low- and high-level cloud layers. Their values for the low-level cloud layers are minimal. These statements are true for all months, seasons and the year as a whole for the both hemispheres.

Long-term monthly (seasonal) means of the number of cloud layers differ little for each atmospheric layer considered in this paper for the Northern and Southern Hemispheres. The minimum values of trends for cloud layers with cloud amount of 0–100% in the atmospheric layers of 0–10, 2–6 and 6–10 km are detected in the cold season and the maximum ones – in the warm season.

Table. The annual mean values and decadal trends of anomalies of the cloud layer number with the cloud amount of 0–100% of the sky surface and intra-annual variations ranges ( $\Delta$ ) of monthly averaged values and decadal trends of their anomalies for different atmospheric layers over the Northern and Southern Hemispheres; changes of cloud layer number for the period 1964–2018. N is the number of soundings.

Atmospheric layer, km	Mean, n	Trends, n/Decade	Changes of the cloud layer number for the period 1964–2018, n	$\Delta$ mean, n	$\Delta$ trends, n/Decade	N, millions
Northern Hemisphere						
0–10	6,4	0,043	0,237	6,33–6,55	0,037–0,046	18,5
6–10	2,3	0,014	0,077	2,25–2,40	0,012–0,015	18,2
2–6	2,8	0,019	0,105	2,66–2,95	0,016–0,021	19,0
0–2	2,1	0,009	0,050	2,10–2,13	0,009	18,1
Southern Hemisphere						
0–10	6,9	0,042	0,231	6,83–6,99	0,039–0,046	3,1
6–10	2,4	0,015	0,083	2,35–2,46	0,014–0,015	3,0
2–6	3,0	0,016	0,088	2,89–3,04	0,015–0,017	3,1
0–2	2,3	0,010	0,055	2,26–2,28	0,010–0,011	3,1

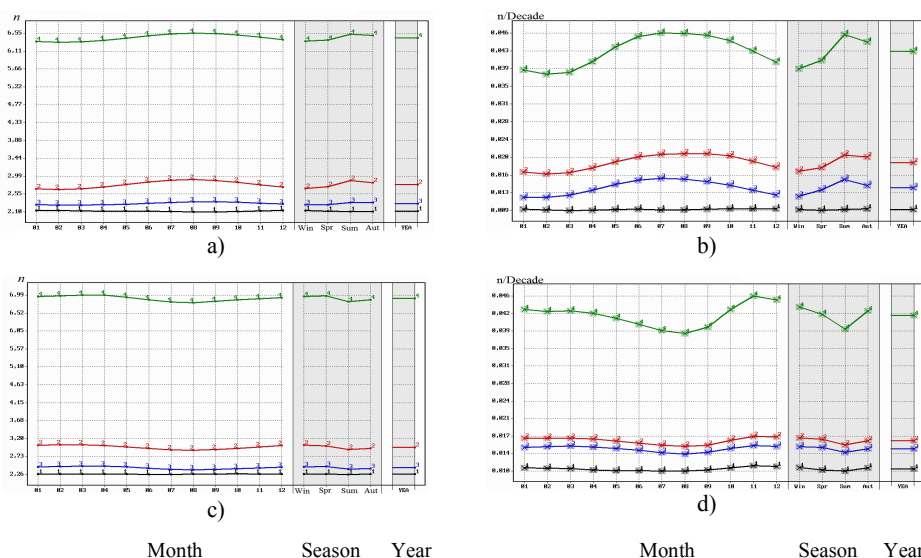


Figure. Long-term means (a, c) and trends of their anomalies (b, d; n per decade) of the number (n) of cloud layers with cloud amount of 0–100% of the sky surface for different atmospheric layers for each month, season and year. The trends with significance of not less than 95% are marked by a square with a cross. Black lines (1) – for 0–2 km, red lines (2) – 2–6 km, blue lines (3) – 6–10 km, green lines (4) – 0–10 km. (a, b) – Northern Hemisphere, (c, d) – Southern Hemisphere. 1964–2018.

## References

1. Chernykh I.V., Aldukhov O.A. Estimating the Number of Cloud Layers through Radiosonde Data from Russian Aerological Stations for 1964–2014 // Russian Meteorology and Hydrology, 2018, Vol. 43, No. 3, pp. 152–160.
2. Chernykh I.V., Aldukhov O.A. Long-term Estimates of the Number of Cloud Layers from Radiosonde Data for 1964–2017 in Different Latitudinal Zones // Russian Meteorology and Hydrology, 2020, Vol. 45, No. 4, pp. 227–238.
3. Chernykh I.V., Aldukhov O.A. Long-term space-time changes in the number of cloud layers reconstructed from radiosonde observations for Russian stations // Proceedings of RIHMI-WDC. 2020. N 187. P. 35–60.
4. Chernykh I.V., Aldukhov O.A., Eskridge R.E. Reply to comments of D.J. Seidel and I. Durre on “Trends in low and high cloud boundaries and Errors in height determination of cloud boundaries” // Bull. Amer. Met. Society. 2003. Vol. 84, No. 2. P.241–247.
5. Chernykh I.V., Eskridge R.E. Determination of cloud amount and level from radiosonde soundings // J. Appl. Meteorol., 1996, vol. 35, pp. 1362–1369.
6. Eskridge R.E., Aldukhov O.A., Chernykh I.V., Zhai P., Polansky A.C., Doty S.R. A comprehensive aerological reference dataset (CARDS): rough and systematic errors // Bull. Amer. Meteor. Soc. 1995. 76. 1759–1775.
7. Rudenkova T.V. Format for archiving of the current aerological data, received from GTS for PC // Proc. RIHMI-WDC, 2010, N 174, p. 41–63.

# Vertical Distribution of Trends of Relative Humidity in the 0-30-km Atmospheric Layer over the Northern and Southern Hemispheres from Radiosounding Data

I. V. Chernykh and O. A. Aldukhov

*Russian Institute of Hydrometeorological Information – World Data Center, Obninsk, Russia, E-mail: [civ@meteo.ru](mailto:civ@meteo.ru), [aoa@meteo.ru](mailto:aoa@meteo.ru)*

## Introduction

The estimations of long-term changes in relative humidity (RH) distributions in the 0-30-km atmospheric layer obtained on the basis of hourly values are necessary for investigations of climate change. The paper presents the series of the first- and second-order trends [1] of relative humidity in the 0-30-km atmospheric layer above the sea level for the Northern (NH) and Southern (SH) Hemispheres for different months and seasons for the period 1964–2018.

## Data and methods

Hourly observations from the CARDS global aerological dataset [2] that were updated by current data from RIHMI-WDC for the period 1964–2018 were used in this research. The necessary condition for including a station in the research was 15-year observations from the full period including 2018. The Akima cubic spline interpolation method was used to calculate RH values and their standard deviations ( $\sigma_{RH}$ ) in the 0–30 km-layer above the sea level taking into account standard levels and specific points of vertical profiles. The linear trends were estimated for each station by using the least squares method. The anomalies were calculated with respect to the corresponding long-term mean values for the period 1964–2018. The statistics obtained for all stations were averaged for the Northern and Southern Hemispheres taking into account the area of the station influence.

## Results

The Figure shows that the spatiotemporal distributions of the first- and second-order trends for the relative humidity anomalies and standard deviations  $\sigma_{RH}$  are nonuniform in the studied layer for the both hemispheres.

The annual changes of the first-order trends of the long-term monthly means anomalies in the 0–30-km layer range from -0.87 to 0.14 and from -0.99 to 0.42 % per decade for RH for the Northern and Southern hemispheres, respectively. The relative humidity decreases at 2–30 km over the Northern hemisphere for all months, the largest RH decrease is detected from December to February at 3–5 km. The relative humidity increases at 0–1 km and at 11–24 km and decreases at 2–8 km over the Southern hemisphere for all months; the largest RH decrease is detected at 3–4 km in summer; the largest RH increase is detected at 0–1 km and at 11–13 km in winter and autumn. The annual changes in the second-order trends of the long-term monthly means anomalies in the 0–30-km layer range from -1.354 to 0.421 and from -0.220 to 1.571 % per decade<sup>2</sup> for RH for NH and SH, respectively. The second-order trends of the long-term monthly means anomalies for RH are positive mostly in the 3–8-km and 0–18-km layers and negative in the 13–30-km and 26–30-km layers for NH and SH, respectively, with significance of more than 95% for all months. Positive values of the second-order trends imply the acceleration of increase in the relative humidity for the cases with positive values of the first-order trends, while this implies the weakening of RH decrease for the case with negative values of the first-order trends, with the year 2018 approaching.

The annual changes in the first-order trends of  $\sigma_{RH}$  in the 0–30-km layer range from -0.061 to 1.724 and from 0.027 to 2.005 % per decade for the Northern and Southern hemispheres, respectively. The first-order trends of  $\sigma_{RH}$  are positive for all months in the entire 2–30 km layer for the Northern hemisphere and in the entire 1–30 km layer for the Southern hemisphere. The most intense increase of  $\sigma_{RH}$  is detected at 9–11 km for the Northern

hemisphere, and throughout the layer 10–12 km over the Southern hemisphere for all months. The annual changes in the second-order trends of  $\sigma_{RH}$  range from -0.822 to 0.617 and from -0.547 to 1.307% per decade<sup>2</sup> for the Northern and Southern hemispheres, respectively.

### Conclusions

The spatiotemporal distributions of the first-order and second-order linear trends of relative humidity anomalies are not uniform in the 0–30-km atmospheric layer over the Northern and Southern Hemispheres. The relative humidity decreases mainly at the heights of 2–8 km over the both hemispheres for all seasons, the positive values of the second-order trends at these heights imply the weakening of the RH decrease, with the year 2018 approaching. The corresponding trends were mainly detected with significance of more than 95%.

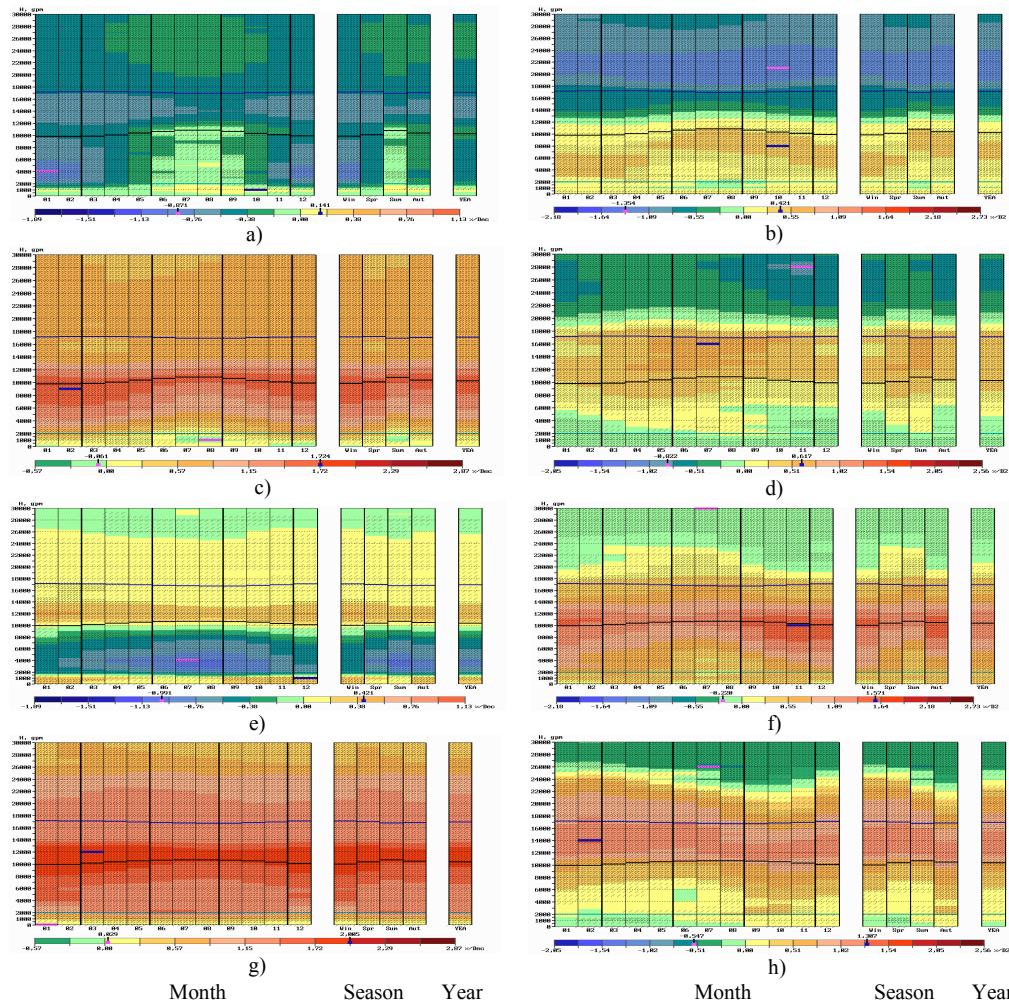


Figure. First-order trends of anomalies of long-term means (a, e) for RH (% per decade), second-order trends of anomalies of long-term means (b, f) for RH (% per decade<sup>2</sup>), and first-order (c, g) and second-order (d, h) trends of standard deviations in the 0–30-km layer for the year as a whole, for each month and season. (a, b, c, d) – Northern Hemisphere, (e, f, g, h) – Southern Hemisphere. Winter – DJF, spring – MMA, summer – JJA, autumn – SON. Blue and pink segments correspond to maximum and minimum values. The statistics for months and seasons were subject to twofold smoothing. The three-points smoothing was used. Trends with significance of not less than 50% are marked by the sloping line segments and those with significance of not less than 95% – by lattice. 1964–2018.

### References

1. Aldukhov O.A., Chernykh I.V. First and second-order trends of air temperature at the surface level from global radiosonde data // Research activities in Earth system modelling. Working Group on Numerical Experimentation. Report No. 50. WCRP Report No.12/2020. Ed.E.Astakhova, July 2020, WMO, Geneva. <http://bluebook.meteoinfo.ru/>, 2020, p. 2-03-2-04
2. Eskridge R.E., et. al. A comprehensive aerological reference dataset (CARDS): rough and systematic errors // Bull. Amer. Meteor. Soc. 1995. **76**. 1759-1775.

## Fourier analysis of climate change in Russia

V.A.Gordin & D.A.Shadrin

National Research University Higher School of Economics  
& Hydrometeorological Center of Russia, Moscow  
123376, Russia. Email: vagordin@mail.ru

The archive of observations of temperature  $f(k)$  at synoptic stations located near major cities of Russia is analyzed. Period: 2001-2020. Observations at the stations are made 8 times a day with a step of 3 hours. In addition, the minimum and maximum temperatures per day are analyzed. At those moments  $k$ , when the measurement result for one or another reason did not get into the archive (for example, the checking algorithm recognized this measurement as erroneous), such a measurement is labeled  $A(k)=0$ . Otherwise, we assume  $A(k)=1$ .

We estimate in each year, in addition to the average temperature, the first Fourier harmonic for seasonal and daily fluctuations. To do this, we introduce a basis of five "almost orthogonal" grid functions (if there are no gaps in the archive of measurements, these functions are  $L^2$ -orthogonal):

$$u_1 = 1, u_2 = \sin(2\pi k / 8), u_3 = \cos(2\pi k / 8), \\ u_4 = \sin(2\pi k / 8N), u_5 = \cos(2\pi k / 8N),$$

where  $N$  is the number of days in a year. Let's determine the best approximation of the function from

$$\text{the measurement data } f(k): \quad f(k) \approx \sum_{j=1}^5 z_j u_j(k),$$

$z_j = \text{const}$ . We define matrix  $Q$  with elements

$$q_{ij} = \frac{\sum_{k=1}^{8N} A(k) u_i(k) u_j(k)}{\sum_{k=1}^{8N} A(k)}, \quad i, j = 1, \dots, 5, \text{ and the vector}$$

$$\vec{Z} \text{ with components } z_i = \frac{\sum_{k=1}^{8N} A(k) u_i(k) f(k)}{\sum_{k=1}^{8N} A(k)}.$$

The best coefficients  $\{b_j\}_{j=1}^5$  are obtained by solution of the SLAE  $Q\vec{b} = \vec{Z}$ . The coefficients providing a minimum of the mean squared deviation

$$\sigma^2 = \sum_{k=1}^{8N} \left[ f(k) - \sum_{j=1}^5 b_j u_j(k) \right]^2$$

are evaluated for any year and for any station. We obtain  $5 \times 20$  values

$\{b_j(m)\}_{j=1}^5$ ,  $m = 1, \dots, M$ , since the archive includes data for  $M=20$  years.

Let us make a transformation for the coefficients  $b_4, b_5$  to evaluate the amplitude of the season temperature dynamics

$$\Theta(m) = \sqrt{b_4^2(m) + b_5^2(m)} \quad \text{and its phase} \\ \Phi(m) = \arctan[b_5(m) / b_4(m)]. \text{ Similarly, we define} \\ \text{the amplitude and phase for the day oscillations:} \\ \mathcal{G}(m) = \sqrt{b_2^2(m) + b_3^2(m)} \quad \text{and} \\ \varphi(m) = \arctan[b_3(m) / b_2(m)].$$

Thus, we obtain 5 functions of the discrete time moment  $m$ :  $g(m): b_1(m), \mathcal{G}(m), \varphi(m), \Theta(m), \Phi(m)$ . Then we construct for every function the best linear approximation:  $g(m) \approx g_0 + g_1 m$ ,  $g_0, g_1 = \text{const}$  by the formulae:

$$g_0 = \frac{1}{M} \sum_{m=1}^M g(m), \quad g_1 = \frac{\sum_{m=1}^M g(m) [m - (M+1)/2]}{\sum_{m=1}^M [m - (M+1)/2]^2}.$$

Here,  $g_0$  is equal to the mean value of the function  $g(m)$  for  $M$  years, and  $g_1$  is its tendency. The mean square deviation of the function is equal to:

$$\sigma_f = \sqrt{\frac{1}{20} \sum_{k=1}^{20} [g(k) - g_0 - g_1 k]^2}.$$

We define the trend as significant if the inequality for its significance of the estimation:  $g_1 M / \sigma \geq 1$  is fulfilled.

Also we evaluated the minimal and maximal (for any day) temperature in a similar way, but without functions  $u_2(k), u_3(k)$ . Let  $t_{fs}(m)$  be the day of the last spring frost ( $t_{\min}^\circ < 0$ ) and  $t_{fa}(m)$  be the day of the first autumn frost in the year  $m$ . We have also evaluated the trends of these dates over 20 years.

**Results** (see Table for some details). The average annual temperature (as well as the average annual  $t_{\min}^\circ(m)$ ) grew in all cities, although not monotonously. The tendencies for  $t_{\max}^\circ(m)$  are not so clear.

The amplitude of seasonal fluctuations decreased in most cities in the middle and high latitudes. In the southern cities (Astrakhan, Stavropol) the amplitude grew. In some cities, the amplitude

trends were not significant. The mean daily amplitude significantly increased in Nizhny Novgorod, Stavropol and Astrakhan.

The time of the last spring and first autumn frosts is important for agriculture and transport. We learn that the trends of these dates have different signs. In most cities, this warm period between these frosts has increased. The most noticeable growth occurred in the northernmost city, Murmansk, where the increase is more than 1 month.

**Conclusions.** Fourier analysis of the series of temperature observations makes it possible to identify both coarse effects (an increase in the average air temperature) and more delicate ones (the amplitude and phase of daily and seasonal fluctuations). In the second case, the results are not so unambiguous and significantly depend on the location of the synoptical station. The same applies to the estimation of the dynamics of the minimal and maximal temperature per day, as well as the days of frost. Such climate changes are useful to take into account when making decisions in agriculture, utilities, transport, construction, medicine, etc.

The table shows the climatic data for megapolises. When analyzing other regions, the results may show different trends. For example, in the small settlement of Barabinsk (Siberia), no significant changes in the average annual temperature were found. More complete information about climate change is expected to be presented in another publication.

We are grateful to A.N.Bagrov for useful discussions and the help in the calculations.

### Literature

[1] S. M. Semenov and E. S. Gelver. Variations in the Yearly Course of Daily Mean Air Temperature over the Russian Territory in the 20th Century. Doklady Earth Sciences, Vol. 386, No. 7, 2002, pp. 846–850. Translated from Doklady Akademii Nauk, Vol. 386, No. 3, 2002, pp.389–394.

[2] V.A.Gordin. About some climatic change in Russia. Research activities in Earth system modelling. Working Group on Numerical Experimentation. Report No. 50. WCRP Report No.12/2020. WMO, Geneva. pp.7.09 – 7.10

Table of tendencies (and the evaluation's significance)

City	Mean annual temperature (degree/year)	Amplitude of seasonal oscillations (degree/year)	Mean annual minimal temperature (degree/year)	Mean annual maximal temperature (degree/year)	Day of the last spring/ first autumn frost (day)	Increase of the warm periods (day)
Moscow	0.081 (3.3)	-0.066 (0.9)	0.085 (3.1)	-0.052 (0.7)	0.015/0.744	14.6
St. Petersburg	0.088 (3.0)	-0.100 (3.4)	0.098 (3.3)	-0.087 (1.2)	0.037/-0.349	-6.2
Penza	0.068 (2.4)	0.006 (0.1)	0.067 (2.1)	-0.009 (0.1)	0.07/0.067	1.2
Ekaterinburg	0.034 (1.0)	-0.002 (0.2)	0.034 (1.0)	0.015 (0.2)	-0.324/-0.123	6.0
Chita	0.056 (1.5)	-0.068 (1.4)	0.052 (1.5)	-0.057 (1.0)	0.133/0.077	-1.1
Khabarovsk	0.054 (1.8)	-0.048 (0.9)	0.157 (6.3)	-0.081 (1.5)	-0.001/0.282	5.6
Vladivostok	0.033 (1.2)	-0.014 (0.3)	0.107 (4.7)	-0.008 (0.2)	0.031/-0.145	-3.5
Magadan	0.063 (3.2)	-0.017 (0.6)	0.121 (5.1)	-0.013 (0.4)	-0.269/0.162	8.6
Stavropol	0.050 (1.7)	0.021 (0.4)	0.017 (0.7)	0.046 (0.8)	-0.03/-0.198	-4.0
Astrakhan	0.050 (2.0)	0.045 (0.8)	0.041 (1.6)	0.044 (0.8)	-0.045/-0.143	-2.0
N.Novgorod	0.053 (2.2)	-0.06 (0.8)	0.042 (1.8)	-0.045 (0.6)	0.074/0.549	9.5
Murmansk	0.054 (1.5)	-0.014 (0.3)	0.05 (1.5)	0.007 (0.1)	-0.824/0.736	31.2

# Interannual variability of ENSO indices and cloud amount over India

Sujata K. Mandke<sup>1,\*</sup> and Amita Prabhu<sup>1</sup>

<sup>1</sup>Indian Institute of Tropical Meteorology, Ministry of Earth Sciences, India

\*amin@tropmet.res.in, amitaprabhu@tropmet.res.in

## Introduction

The present study analyses the interannual variability and trends in El Niño Southern Oscillation (ENSO) indices as well as cloud amount averaged over India, for the period 1984-2009. The low-level and mid-level clouds are considered. Trends in cloud cover over different regions of the world examined by several researchers indicated that trends are neither uniform everywhere, nor same across different time periods over some regions (Jaswal, 2017 and references therein). Annual and seasonal trends in total cloud cover over India based on the period 1951-2010 are decreasing (Jaswal, 2017), the mechanism for which is still unknown. Trends in cloud cover over some of the regions are linked to factors such as ENSO (Warren et al. 2007) and aerosols (IPCC, 2007). The relationship between ENSO and cloud amount averaged over India is still not adequately clear and thus examined in the present study.

## 2. Data

The following datasets are used in this study: (i) Cloud amount from the International Satellite Cloud Climatology Project (ISCCP) D2 data (Rossow and Schiffer, 1999), provided for each 280-km grid cell over the globe, for the period from July 1983 to December 2009. The cloud amount (%) is the fractional area covered by clouds observed from the satellites. Low-level and mid-level clouds are classified using their radiance-derived cloud top pressure as per ISCCP cloud classification (<http://isccp.giss.nasa.gov/cloudtypes.html>). (ii) ENSO indices are obtained using optimally interpolated monthly global SST ( $1^\circ \times 1^\circ$ ) version 2, from National Oceanic and Atmospheric Administration (Reynolds et al., 2002).

## Results

The nature of ENSO is commonly quantified using sea surface temperatures (SST) anomalies in the different parts of equatorial Pacific Ocean. The indices of ENSO computed from the standardised SST anomalies averaged over four Niño regions (Trenberth and Stepaniak, 2001), namely Niño1+2 ( $0-10^\circ\text{S}$ ,  $90^\circ\text{W}-80^\circ\text{W}$ ), Niño3 ( $5^\circ\text{N}-5^\circ\text{S}$ ,  $150^\circ\text{W}-90^\circ\text{W}$ ), Niño3.4 ( $5^\circ\text{N}-5^\circ\text{S}$ ,  $170^\circ\text{W}-120^\circ\text{W}$ ) and Niño4 ( $5^\circ\text{N}-5^\circ\text{S}$ ,  $160^\circ\text{E}-150^\circ\text{W}$ ), for the period 1984–2009 are considered in this study and hereafter referred as ENSO indices. Year-to-year variations (solid line with marker) along with the trend (red dashed line) of these four ENSO indices for the period 1984–2009 are illustrated in Figure 1(a-d) respectively. Likewise, cloud amount variations averaged over Indian region [ $8^\circ-38^\circ\text{N}$ ,  $68^\circ-98^\circ\text{E}$ ] (solid line with marker) is depicted with trend (red dashed line) for low-level and mid-level clouds for the period 1984–2009 in Figure 1(e-f) respectively. Small decrease in the year-to-year variability of ENSO indices after 2000 is apparent over all four Niño regions (Figure 1(a-d)). Statistical significance of trend is checked using F-test statistic (Kendall and Stuart, 1979). Trend in four ENSO indices is insignificant (Figure 1(a-d)). An increasing trend in both low-level and mid-level cloud amount averaged over India is significant at 95% confidence level (Figure 1(e-f)). Next, correlation coefficient (CC) between each of the ENSO indices (Niño1+2, Niño3, Niño3.4 and Niño4) is evaluated separately with detrended low-level cloud (green) and also with the mid-level cloud (maroon) amount averaged over the Indian region [ $8^\circ-38^\circ\text{N}$ ,  $68^\circ-98^\circ\text{E}$ ], for summer monsoon season (June-September), based on the period 1984-2009 (Figure 1(g)). Significant inverse relation between four ENSO indices with mid-level cloud amount (Figure 1(g)) suggests that ENSO may be one of the factors causing its increasing trend. The relation between four ENSO indices with low-level cloud amount over India is insignificant. Further efforts are needed to investigate the mechanisms pertaining to increasing trend in low-level cloud amount over India.

## References

- Jaswal, A. K., 2017. Variability and Changes in Cloud Cover Over India During 1951–2010, chapter 7, in book “Observed climate variability and change over the Indian region”, Rajeevan M. and Shailesh Naik (Ed). Springer, Singapore, 107-127.
- IPCC, 2007. Climate change 2007. the physical science basis, contribution of working group I to the fourth assessment report of the IPCC, Cambridge University Press, Cambridge.
- Kendall, M.G., Stuart, A., 1979. The Advanced Theory of Statistics In: Inference and Relationship, Griffin, fourth ed., vol. 2. Hodder Arnold, London, ISBN 0852642555, 758.
- Reynolds, R.W., Rayner, N.A., Smith, T.M., Stokes, D.C., Wang, W., 2002. An improved in situ and satellite SST analysis for climate. *J. Climate* 15:1609–1625.
- Rossow, W. B., and Schiffer, R.A., 1999. Advances in understanding clouds from ISCCP. *Bull. Am. Meteorol. Soc.* 80:2261-2288.
- Trenberth, K. E., Stepaniak, D. P., 2001. Indices of El Niño Evolution. *J. Climate* 14:1697-1701.
- Warren, S. G., Eastman, R. M. and Hahn, C. J., 2007. A survey of changes in cloud cover and cloud types over land from surface observations, 1971-1996. *J. Climate* 20:717-738.

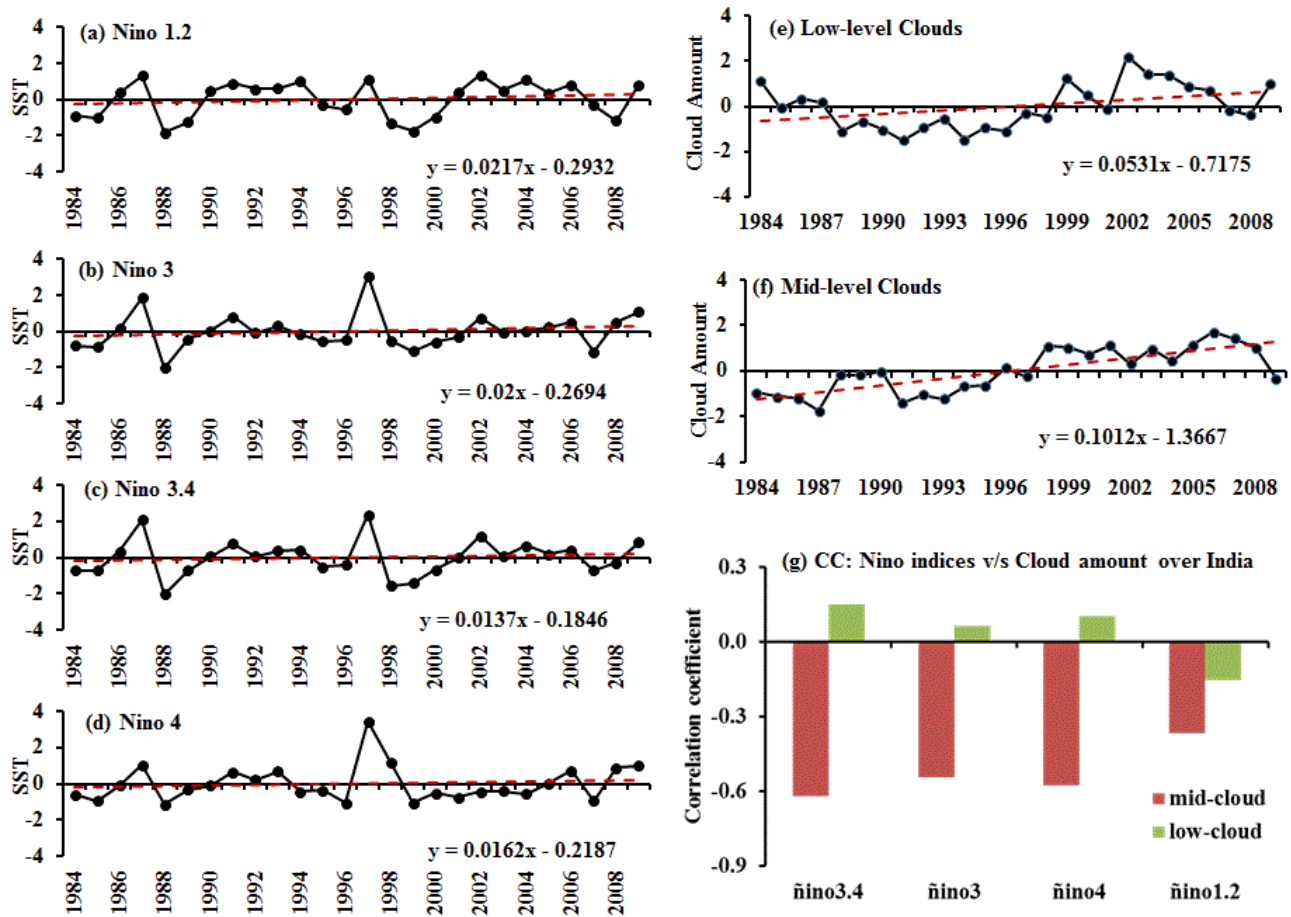


**Figure 1:** (a) Inter-annual variability of Niño1+2 SST index (solid line with marker) along with the linear trend (red dashed line) for the period 1984-2009. (b)-(d) same as Figure 1(a) except for Niño3, Niño3.4 and Niño4 SST indices respectively. (e) Inter-annual variability of low-level cloud amount (%) (solid line with marker) averaged over the Indian region [8°-38°N,68°-98°E] along with the trend (red dashed line) for the period 1984-2009. (f) same as Figure 1(e) except for mid-level cloud amount. (g) Correlation coefficient between each of ENSO indices (Niño1+2, Niño3, Niño3.4 and Niño4) separately with detrended low-level cloud (green) and mid-level cloud (maroon) amount averaged over the Indian region [8°-38°N,68°-98°E], based on the period 1984-2009.

## Changes in the hydrological cycle in the Caspian Sea basin in recent decades

Mokhov I.I.<sup>1,2</sup>, Klimovich G.P.<sup>2</sup>

<sup>1</sup>A.M. Obukhov Institute of Atmospheric Physics RAS

<sup>2</sup>Lomonosov Moscow State University

mokhov@ifaran.ru

This paper is related to the analysis of changes in the hydrological cycle in the Caspian Sea basin and their connection to the key modes of climate variability based on observational data over the past decades. The Caspian Sea is the largest lake in the world, and one of the largest regional climatic variations over the last century is associated with the large Caspian Sea level (CSL) anomalies and regional variations in the hydrological cycle (Arpe et al., 2000). The analysis used monthly-mean values for the Caspian Sea level (CSL) ([http://esimo.ru/dataview/viewresource?resourceId=RU\\_RIHMI-WDC\\_663&armId=casp](http://esimo.ru/dataview/viewresource?resourceId=RU_RIHMI-WDC_663&armId=casp)), as well as monthly-mean values for the rivers runoff by the data available at the State Hydrological Institute (<http://www.hydrology.ru/>). Also, the monthly-mean values of the indices characterizing the North Atlantic Oscillation (NAO) and El Niño/Southern Oscillation (Nino3, Nino3.4, Nino4, SOI) were used ([https://psl.noaa.gov/gcos\\_wgsp/Timeseries/](https://psl.noaa.gov/gcos_wgsp/Timeseries/)).

Figure 1 shows the interannual variations in the CSL for the period 1900–2020 compared with moving 30-year changes in the winter NAO index.

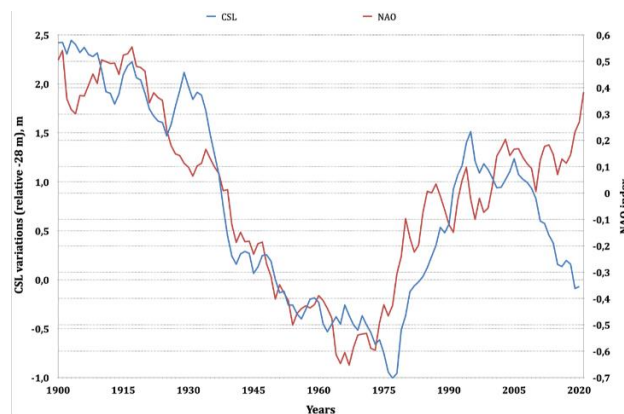


Figure 1. Interannual CSL variations (blue curve) for the period 1900–2020. Moving 30-year changes in the winter NAO index are also noted (red curve).

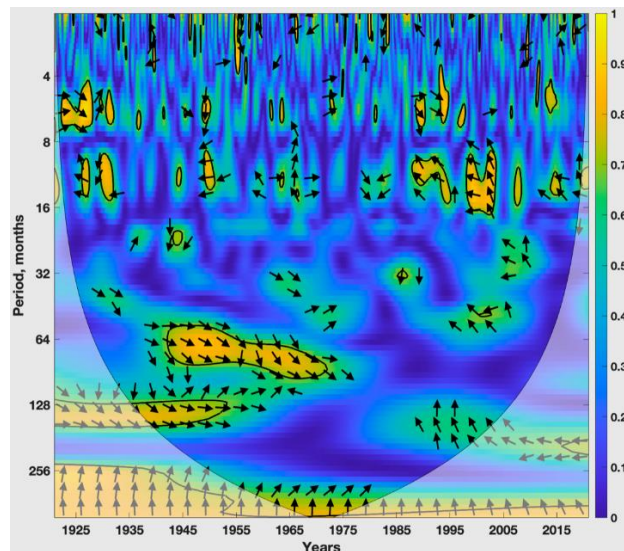


Figure 2. Local coherence of CSL anomalies (at Krasnovodsk station) with the NAO index by monthly-mean data for the period 1921–2020. Regions of significant coherence (at the level of 95%) are highlighted; the arrows show the phase shift (arrow to the right denotes in-phase, to the left, antiphase); regions of boundary effects are also indicated.

Figure 2 with the results of a cross wavelet analysis of GSL variations (at Krasnovodsk station) and NAO index by monthly-mean data for the period 1921-2020 shows significant local coherence for long-term variations.

For the last decades, a significant coherence of CSL with El Niño phenomena has been also noted for long-term variations with periods of about three decades or more. This coherence is more significant with El Niño events, with the strongest surface temperature anomalies at equatorial latitudes in the central Pacific Ocean. Also, a significant coherence for interdecadal and intradecadal variations was noted.

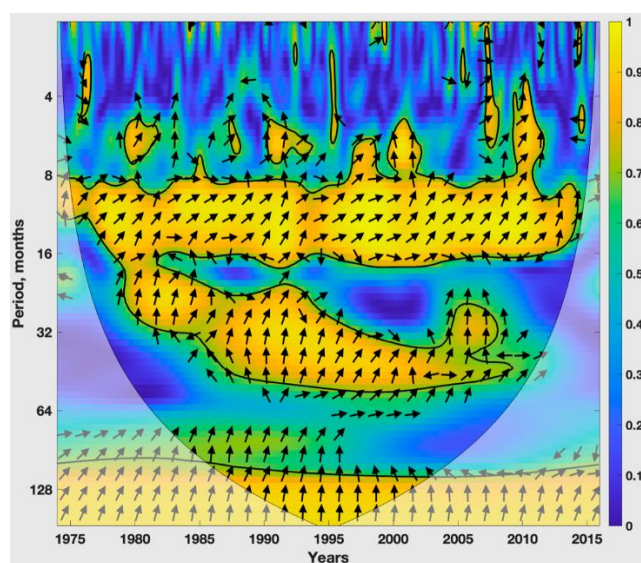


Figure 3. Local coherence of the CSL and Volga River runoff by monthly-mean data for the period 1974–2015.

According to the results of cross-wavelet analysis in Fig. 3, the local coherence of the CSL and the Volga River runoff by monthly-mean data is significantly manifested in the annual cycle. Also, their coherence for interannual and interdecadal variations was noted. Local coherence of the CSL and the Ural River runoff for the period 1938-2016 (not shown) manifests itself significantly in the annual cycle and is much weaker for interannual and interdecadal variations. The runoff of the Volga and Ural rivers shows statistically significant coherence in the annual cycle but has no significant coherence of interannual and interdecadal variations over the past decades.

This work was supported by the Russian Science Foundation (project 19-17-00240).

## References

Arpe K., Bengtsson L., Golitsyn G.S., Mokhov I.I., Semenov V.A., Sporyshev P.V. Connection between Caspian Sea level variability and ENSO. *Geophys. Res. Lett.*, 2000, **27**, 2693-2696.

# Regional temperature anomalies and accompanying processes in connection with the longest La Niña in 1908-1911

Mokhov I.I.

A.M. Obukhov Institute of Atmospheric Physics RAS  
Lomonosov Moscow State University  
mokhov@ifaran.ru

The strongest interannual variations of global temperature at the surface are associated with the El Niño and La Niña events. Differences in the probabilities of anomalously warm and anomalously cold winters in the El Niño and La Niña phases for the North Eurasia regions are noted (Mokhov, 2020). Significant changes are noted for El Niño and La Niña frequency and duration during past decades (Mokhov, 2022; Mokhov and Medvedev, 2022).

Figure 1 shows estimates of the El Niño/La Niña periods by the data for the Niño3 index ([https://psl.noaa.gov/gcos\\_wgsp/Timeseries/](https://psl.noaa.gov/gcos_wgsp/Timeseries/)) for the period 1870–2020 with the largest variations at the beginning of the 20<sup>th</sup> century (Mokhov and Medvedev, 2022). According to (Wolter and Timlin, 2011) La Niña events can last longer than El Niño, exceeding 40 months for the 1908-1911 La Niña.

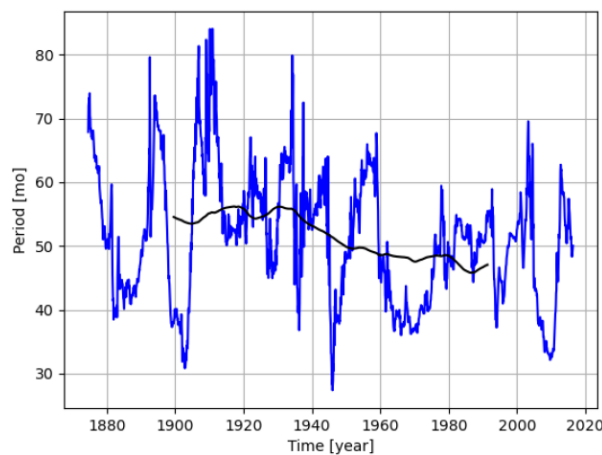


Figure 1. Estimates of the length of El Niño/La Niña periods (months) on moving intervals  $I_0 = 84$  months for the period 1870–2020 using the Niño3 index, smoothed with a window length  $I_s = 24$  months. The black curve corresponds to a 50-year moving average periods.

Figure 2 shows annual-mean anomalies for the temperature near surface in the eastern part of the Northern Hemisphere in 1909 and 1910 by GISS data (<https://data.giss.nasa.gov/gistemp/>) during the longest La Niña 1908-1911. The largest negative anomalies were noted for northern Asian regions, especially in 1910.

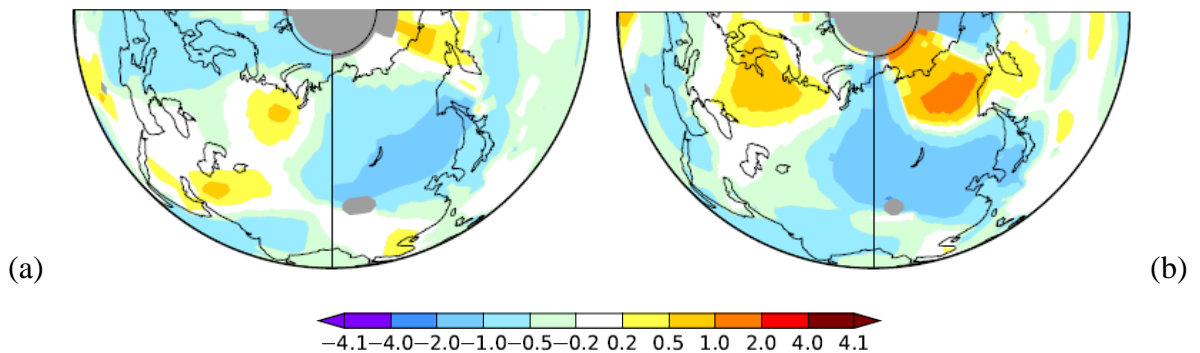


Figure 2. Annual-mean temperature anomalies (°C) in 1909 (a) and 1910 (b) relative the 1951-1980 period.

More detail seasonal features are presented on Fig. 3 for temperature anomalies in 1910. Negative temperature anomalies in all seasons were noted in the Far East with the strongest negative temperature anomalies in winter.

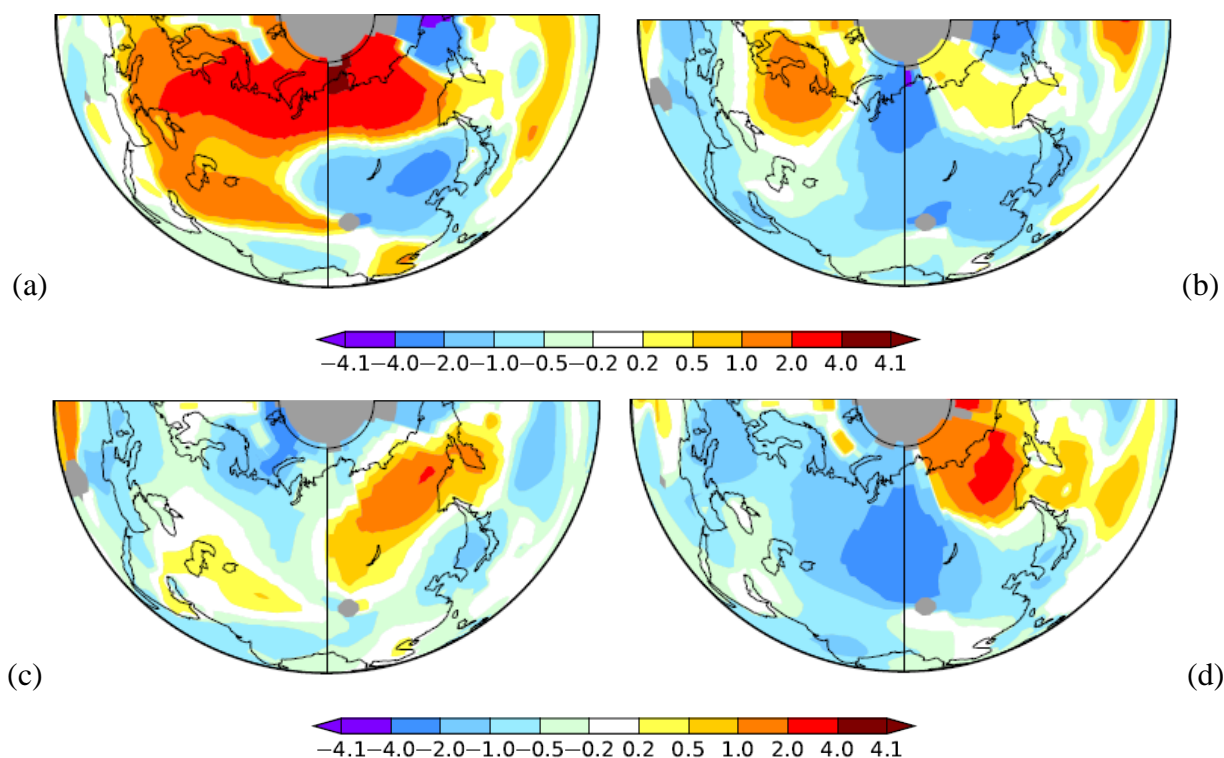


Figure 3. Seasonal temperature anomalies ( $^{\circ}\text{C}$ ) in 1910 (relative to 1951-1980): (a) Winter, (b) Spring, (c) Summer, (d) Autumn.

Regional temperature anomalies during the record-breaking La Niña in 1908-1911 should be accompanied by significant consequences. It is worth noting that during the longest La Niña in 1910-1911, a plague epidemic broke out in the eastern Asian regions, in particular in the Far East (Kastorsky, 1911). According to (Suntsov, 2019), climate cooling with the deeper soil freezing affects ecological processes and the life cycle of potential plague pathogens, in particular in Asian regions.

This work was supported by the Russian Science Foundation (project no. 19-17-00240).

## References

- Kastorsky E.S. Epidemic of Pneumonic Plague in the Far East in 1910-1911 and Measures to Combat It. Irkutsk. 1911. 115 pp. (in Russian)
- Mokhov I.I. Anomalous winters in regions of Northern Eurasia in different phases of the El Nino phenomena. *Doklady Earth Sci.*, 2020, 493 (2), 649-653.
- Mokhov I.I. Changes in the frequency of phase transitions of different types of El Niño phenomena in recent decades. *Izvestiya, Atmos. Oceanic Phys.*, 2022, **58** (1), 1–6.
- Mokhov I.I., Khvorostyanov D.V., Eliseev A.V. Decadal and longer term changes in El Niño - Southern Oscillation characteristics. *Intern. J. Climatol.*, 2004, **24**, 401-414.
- Mokhov I.I., Medvedev N.N. Features of El Niño phenomena of various types and their changes in recent decades. *Moscow University Physics Bulletin*, 2022, **77** (3).
- Suntsov V.V. Origin of the plague: prospects of ecological-molecular-genetic synthesis. *Herald Rus. Acad. Sci.*, 2019, 89 (3), 271-278.
- Wolter K., Timlin M.S. El Niño/Southern Oscillation behaviour since 1871 as diagnosed in an extended multivariate ENSO index (MEI.ext). *Intern. J. Climatol.*, 2011, **31**, 1074–1087.

# Estimates of the relationship between the atmospheric pressure variability and the frequency of hospitalizations

Mokhov I.I.<sup>1,2</sup>, Matesheva A.V.<sup>1</sup>

<sup>1</sup>A.M. Obukhov Institute of Atmospheric Physics RAS

<sup>2</sup>Lomonosov Moscow State University

mokhov@ifaran.ru

Weather, climatic and environmental factors affect the conditions (health) of people with an abnormal level of functioning of the adaptive system and increased meteosensitivity, patients with chronic diseases, including hypertension and coronary heart disease. An analysis of the relationship between the frequency of emergency hospitalization of meteosensitive patients and the atmospheric pressure variability was carried out. In this case, data on hospitalizations at the Central Clinical Hospital of the Russian Academy of Sciences (CCH RAS) in Moscow and data on atmospheric pressure fluctuations were used [1]. Atmospheric pressure fluctuations in [1] were determined from measurements with a liquid microbarograph with a time step of 0.5 sec. and meteorological barograph.

The monograph [1] presents the data on emergency hospitalizations in the CCH RAS of more than 6 thousand weather-dependent patients for the period from the beginning of 2009 to the end of 2012. Patients were diagnosed with a myocardial infarction, angina pectoris, hypertensive crisis, extrasystole, acute violation of cerebral circulation, cerebrovascular disease. Some patients respond to a decrease in pressure, some to an increase. Different types of dependence of the number of patients on the rate of pressure change, on acceleration and on the absolute level of atmospheric pressure were manifested.

Figure 1 shows local coherence of the frequency of hospitalizations in the CCH RAS with the atmospheric pressure according to daily data during 04.08.2009-29.10.2009. For the entire analyzed period, there was a significant coherence for the longest-term variations - with a period of about a month or more. Until the second decade of September 2009, there was also coherence for variations with periods of more than a week – up to two weeks. The change in coherence is affected by the change in weather and climate conditions, including autumn regimes such as Indian Summer.

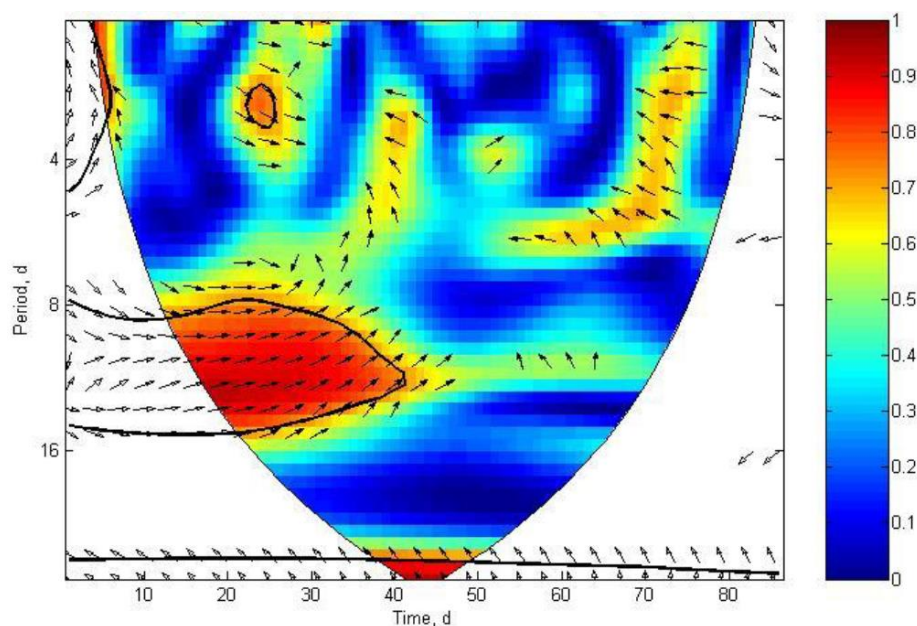


Figure 1. Local coherence of the frequency of hospitalizations in the CCH RAS with atmospheric pressure by daily data during 04.08.2009-29.10.2009. Regions of significant coherence (at the level of 95%) are highlighted; the arrows show the phase shift (arrow to the right denotes in-phase, to the left, antiphase); regions of boundary effects are also indicated.

An extreme weather and climate regime under conditions of atmospheric blocking formed in the European part of Russia in the summer of 2010 with record heatwave, forest fires, haze, and air pollution, which caused huge social, environmental, and economic losses [2,3]. Figure 2 presents local coherence of frequency of hospitalizations in the CCH RAS with atmospheric pressure by daily data during July 2010.

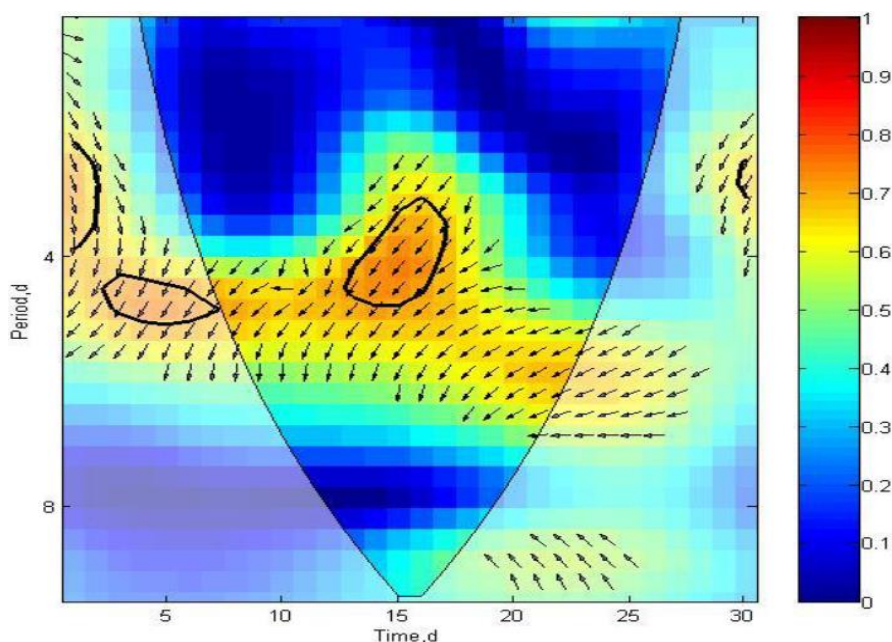


Figure 2. Local coherence of frequency of hospitalizations in the CCH RAS with atmospheric pressure by daily data during July 2010.

Figures 1 and 2 display different connections of frequency of hospitalizations in the CCH RAS with atmospheric pressure during 04.08.2009-29.10.2009 in July 2010. The figures demonstrate the differences both for periods of significant coherence and for phases between pressure fluctuations and frequency of hospitalizations. According to [1] in the summer of 2010 in Moscow, due to record heatwave and air pollution, the frequency of strokes, hypotension, respiratory diseases, in contrast to cardiovascular diseases, increased significantly.

This work was supported by the Russian Science Foundation (project 19-17-00240)

## References

1. Health of the Population of Russia: The Impact of the Environment in a Changing Climate. Moscow, Nauka, 2014, 428 p. (in Russian)
2. The State of the Air Basin of Moscow in Extreme Weather Conditions in the Summer of 2010. All-Russian Meeting. Moscow, A.M. Obukhov Institute of Atmospheric Physics RAS, 2010, 100 p. (in Russian)
3. Analysis of Abnormal Weather Conditions on the Territory of Russia in the Summer of 2010. Moscow, Triada LTD, 2011, 72 p. (in Russian)

# Seasonal features of Snow Cover Extent variations in Eurasia in the annual cycle and their changes over the decades

M. Parfenova<sup>1</sup>, M. Arzhanov<sup>1</sup>, I.I. Mokhov<sup>1,2</sup>

<sup>1</sup> *A.M. Obukhov Institute of Atmospheric Physics RAS*

<sup>2</sup> *Lomonosov Moscow State University*

Being a crucial part of the climatic system, the snow cover extent (SCE) is sensitive to the ongoing warming. The observed increased variability of the SCE in the recent decades is manifested in intensification of extreme weather events compared to previous years. In this paper, we analyze the interseasonal and interannual variability of SCE and the features of its changes over the last four decades using the satellite data and the results of the numerical simulations of the SCE in Eurasia with the models of the CMIP6 project (<https://esgf-node.llnl.gov/projects/cmip6>).

Figure 1 presents phase portraits for the SCE in the Northern Hemisphere based on monthly average satellite data for the two sub-periods: 1979-1999 and 2000-2020. The corresponding averaged phase portraits for 20-year periods of 1980-1999 and 2000-2019 are marked in bold. According to the satellite data for the analyzed 40-year period, the average annual snow cover extent in the Northern Hemisphere is about 25 million km<sup>2</sup>. The maximum area of snow cover in the NH in the annual course is about 50 million km<sup>2</sup>, the minimum is less than 3 million km<sup>2</sup>.

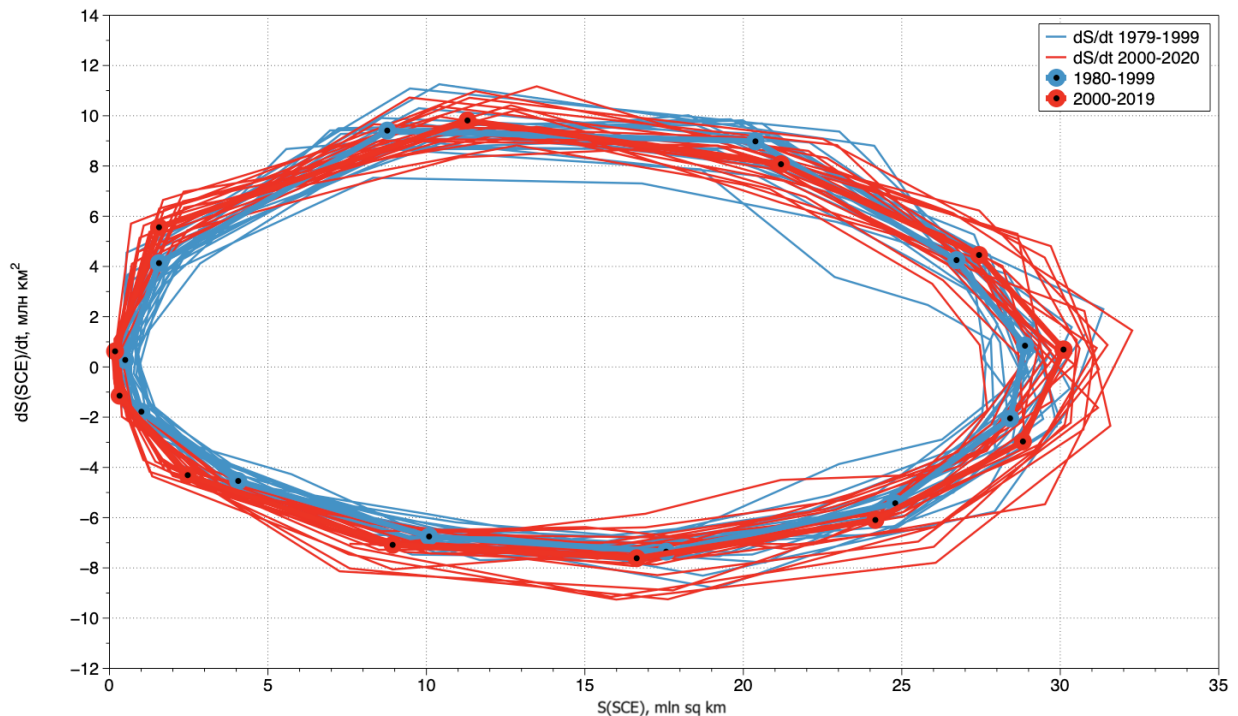


Figure 1 Phase portraits for snow cover extent in Eurasia based on satellite monthly average data for two sub-periods: 1979-1999 (blue color) and 2000-2020 (Red color). The corresponding monthly averaged phase portraits for 20-year periods of 1980-1999 and 2000-2019 are marked in bold.

The greatest variability of the snow cover area is manifested in the coldest months with the greatest extent of the snow cover. For the summer months, the variability of the snow cover area is noticeably less, while the tendency for a decrease in the snow cover area with general warming in recent decades is more pronounced for them than for the winter months.

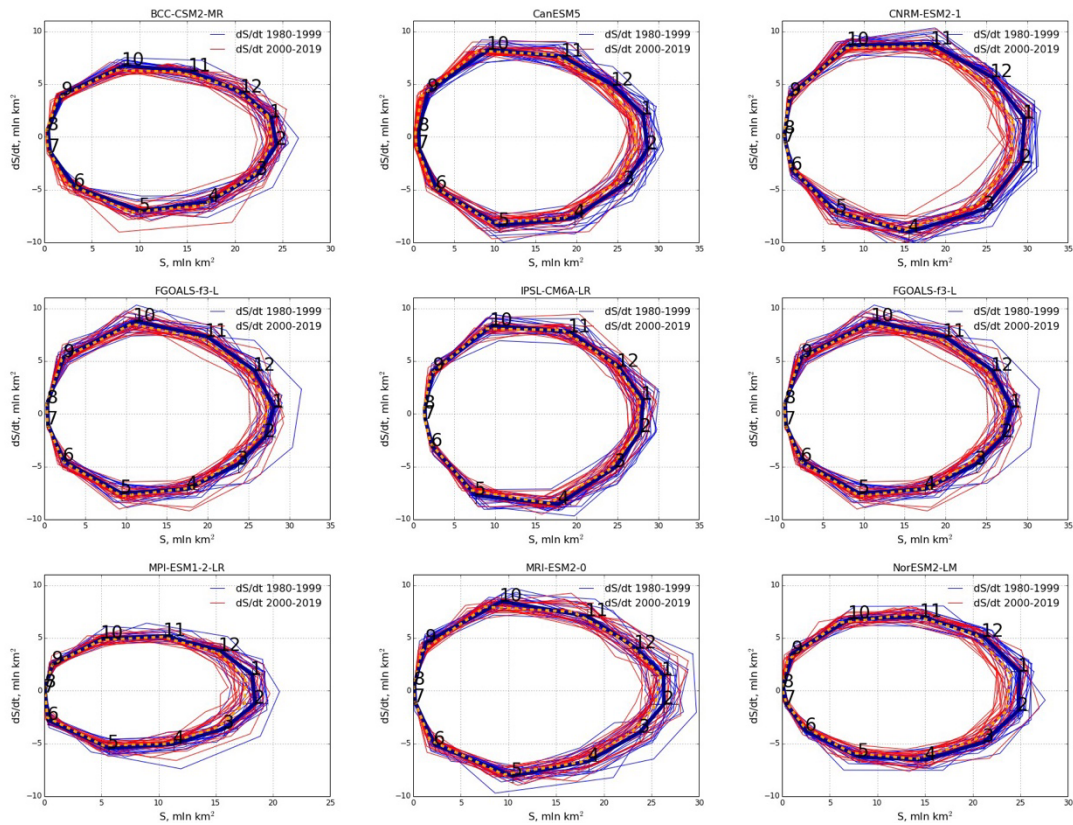


Figure 2 Phase portraits for snow cover extent in Eurasia based on the results of models simulations monthly averaged data for two sub-periods: 1980-1999 (blue color) and 2000-2019 (Red color). The numbers represent the months from January to December (1-12 respectively).  $S = S(\text{SCE})$ .

Figure 2 presents the phase portraits for the results of numerical simulations of the snow cover extent by the models of CMIP6 project for the same time periods. It is seen that the SCE variability in the winter months is also significantly greater than that in the summer months. While some of the models reproduce the results of satellite data analysis well, others tend to underestimate the variability for the most recent time period.

The increase of SCE in the autumn months during warming can be explained by an increase in the transport of water vapor in the atmosphere with snowfall over the continents due to a decrease in the area of sea ice in the Arctic Ocean. It is significant that for the modern climate of recent decades, in particular for Eurasia, it is in October that a transition to negative surface temperatures and the formation of snow cover starts.

Features of snow cover changes can be associated not only with long-term trends in climate change and modes of interdecadal and intradecadal climatic variability, which manifest themselves differently in different regions, but also with the features of the analyzed data and its homogeneity, including CDR satellite observation data. In particular, the need to correct the CDR data until 2005 was noted in several papers.

This work was supported by the Russian Science Foundation (project 19-17-00240).

## References

1. Mokhov I.I. Diagnostics of the Climatic System Structure. Gidrometeoizdat, St. Petersburg, 1993. [in Russian]
2. Mokhov I.I., Parfenova M.R. changes in the snow cover extent in Eurasia from satellite data in relation to hemispheric and regional temperature changes // Doklady Earth Sciences, 2021, **501**, № 1, 963-968. DOI:10.1134/S1028334X21110106

## Cloud climatology from ISCCP data

Amita Prabhu<sup>1,\*</sup> and Sujata K. Mandke<sup>1</sup>

<sup>1</sup>Indian Institute of Tropical Meteorology, Ministry of Earth Sciences, India

\*[amitaprabhu@tropmet.res.in](mailto:amitaprabhu@tropmet.res.in), [amin@tropmet.res.in](mailto:amin@tropmet.res.in)

### 1. Introduction

Clouds are crucial component of Earth's climate due to their important role in the radiative balance and hydrological cycle. Cloud climatologies have been developed from two types of data sources; one from satellites and the other from ground-based and aircraft observations. The ground-based and aircraft data is greatly limited by the amount of temporal and spatial coverage compared to satellite observations that provide continuous data over entire globe across the wide range of spatial and temporal scales. Most of the earlier cloud climatologies derived from surface observations (Eastman et al., 2011) and satellite data (Miller and Feddes, 1971) have reported on the cloud amount only, while studies of other cloud properties such as cloud top temperature climatology are lacking. Nonetheless, changes in cloud-type (such as cloud-top height and water content) may well affect radiation field as much as variations of cloud amount (Chen et al., 2000). The radiative forcing of variety of cloud types is different (Hartmann et al., 1992) depending on the properties of clouds namely thickness, height, water or ice content and shape. For example, the abundant low-level clouds provide the largest contribution to the net energy balance of the Earth on a global average basis, thereby exerting strong cooling effect due to high albedo (Hartmann et al., 1992), while mid-level clouds display varied radiative effects (Sassen and Wang, 2012). Based on the above scientific background, climatology of cloud amount and cloud top temperature from International Satellite Cloud Climatology Project (ISCCP) data is studied for both low-level and mid-level clouds in the present paper.

### 2. Data

The International Satellite Cloud Climatology Project (ISCCP) (Rossow and Schiffer, 1999) D2 data is used, which provides global monthly cloud type amount and other cloud characteristics reported in a 280-km equal area box from July 1983 to December 2009. The cloud amount (%) represents the fractional area covered by clouds as observed from the satellites. The cloud amount is estimated by evaluating each pixel of 5 km across for a particular level by counting the number of pixels that are marked as cloudy and dividing by the total number of pixels in a region of about 280 km across. Low-level and mid-level clouds are classified using their radiance-derived cloud top pressure as per ISCCP cloud classification (<http://isccp.giss.nasa.gov/cloudtypes.html>). A detailed description about the classification of clouds and cloud amount computation at High, Mid and Low levels is available from the ISCCP report (<http://isccp.giss.nasa.gov/products/products.html>).

The climatology of cloud amount and cloud top temperature based on the period 1984-2009, for four seasons defined as average over December-January-February (DJF), October-November (ON), June-July-August-September (JJAS) and March-April-May (MAM) is obtained in this study.

### 3. Results

Climatology of cloud amount is illustrated over 0-360°; 40°S-40°N for four seasons namely MAM, JJAS, ON and DJF respectively in Figure 1, I(a-d) for low-level clouds and in Figure 1, II(a-d) for mid-level clouds. Likewise, cloud top temperature climatology is shown in Figure 1, III(a-d) and Figure 1, IV(a-d) for low-level and mid-level clouds respectively. Cloud amount climatology of low-level and mid-level clouds during all the four seasons reveal predominance of low-level clouds over the ocean while mid-level clouds dominate over the land, except during JJAS season, when mid-level clouds are present over tropical oceans also. Seasonal variations in low-level cloud amount are small, except over North America, North Africa and Australia (Figure 1, I(a-d)). Mid-level cloud amount demonstrates seasonal variations only over North America and Asia (Figure 1, II(a-d)).

Cloud top temperature climatology of both low-level clouds (Figure 1, III(a-d)) and mid-level clouds (Figure 1, IV(a-d)) indicates high temperatures (270 K- 280 K) over tropics, with seasonal movement of clouds having high top temperature toward mid-latitude in the respective summer hemisphere. Considerable seasonal changes in cloud top temperature of low-level clouds over North America, North Africa, Asia and Australia are evident (Figure 1, III(a-d)).

## References

- Chen, T., Rossow, W. B. and Zhang, Y., 2000. Radiative effects of cloud- type variations, *Journal of Climate*, 13:264–286.
- Eastman, R., Warren, S. G. and Hahn, C. J., 2011. Variations in Cloud Cover and Cloud Types over the Ocean from Surface Observations, 1954–2008, *Journal of Climate*, 24:5914-5934.
- Hartmann, D. L., Ockert-Bell, M. E. and Michelsen, M. L., 1992. The effect of cloud type on Earth’s energy balance: Global analysis. *Journal of Climate*, 5:1281–1304
- Miller, D. B. and Feddes, R. G., 1971. Global atlas of relative cloud cover. AD739434-Rept. 1, U.S. National Environmental Satellite Service and USAF Environmental Technical Applications Center, Washington, D.C.
- Rossow, W. B. and R. A. Schiffer, 1999. Advances in understanding clouds from ISCCP, *Bulletin of American Meteorological Society*, 80:2261 – 2288.
- Sassen, K. and Wang, Z., 2012. The Clouds of the Middle Troposphere: Composition, Radiative Impact, and Global Distribution, *Surveys in Geophysics*, 33:677–691

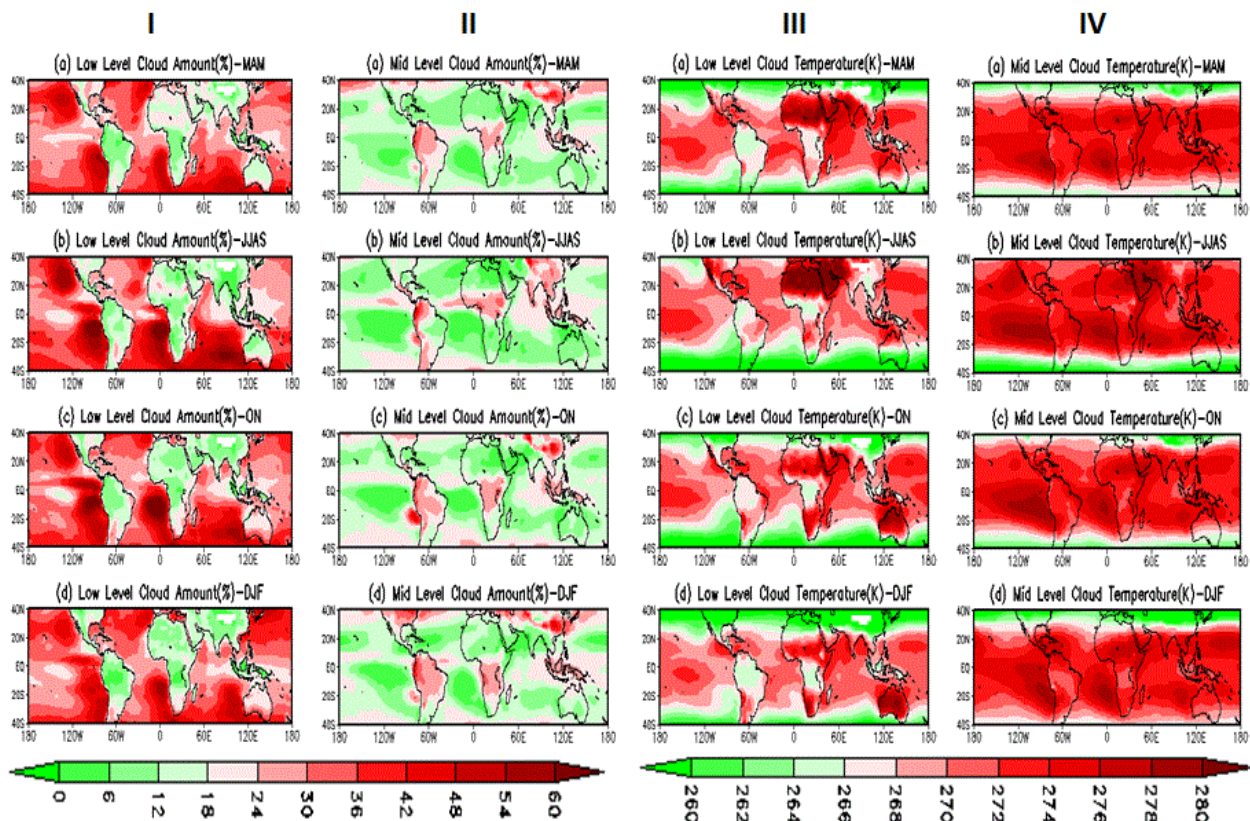


**Figure 1.**

- I.** Spatial plot of climatology of low-level cloud amount (%) averaged over four seasons :  
 (a) March-May (MAM) (b) June-September (JJAS) (c) October-November (ON) (d) December-February (DJF)
- II.** (a, b, c, d). same as Figure 1 (I a, b, c, d) respectively except for mid-level cloud amount.
- III.** (a, b, c, d). same as Figure 1 (I a, b, c, d) respectively except for low-level cloud top temperature.
- IV.** (a, b, c, d). same as Figure 1 (III a, b, c, d) respectively except for mid-level cloud top temperature.

# Analysis of deep convection distribution in the middle latitudes of Europe using satellite data and the European Severe Weather Database

Shishov A.E.

The Hydrometcentre of Russia, 123376 Moscow, Russia, B. Predtechensky per.  
shandruha@gmail.com

In order to study rapidly developing mesoscale phenomena like deep convection clouds (also referred to as deep convection objects or, briefly, DCOs), characterized by high variability through both time (from 15 minutes to 3 days) and space (1- 600 km or more in diameter), a long series of continuous geostationary satellite observations with a high spatial resolution (~5 km) and a low repeat cycle (15 minutes) was analyzed. Only latitudes from 40 to 72 degrees north and longitudes from 20 to 65 degrees east for the period of 2013-2021 (from April to September) were considered.

The presented paper is dedicated to two goals.

1) A study of DCO frequency in the midlatitude regions of Europe based on satellite data in the three infrared channels: 10.8, 6.2, and 7.3  $\mu\text{m}$ . The brightness temperature  $T_{10.8}$  provides an estimate of DCO cloud top temperature and height; the brightness temperature difference  $T_{6.2} - T_{10.8}$  describes cloud thickness; the brightness temperature difference  $T_{6.2} - T_{7.3}$  describes the thickness of the upper part of a DCO.

2) A verification of a DCO detection algorithm based on satellite imagery against two databases: surface synoptic observations (SYNOP) and reports of categories QC1 (verified by a reliable source) and QC2 (scientific case study) from the European Severe Weather Database (ESWD) [3].

Although modern DCO detection algorithms based on satellite imagery are known to suffer from high false alarm rates (20-63%, depending on detection method, dataset, and validation approach), they are still useful in detection and tracking tasks, since satellite data provide valuable information about DCO lifecycle, size, and cloud top texture [1,2]. Hence, the first stage of our analysis involved calculation of the following DCO features: lifetime (DCO tracking duration in hours) and maximum size (maximum area in sq. km of DCO cloud top region with temperatures below -50 degrees Celsius).

In total, 10 683 356 unique DCOs were detected using a thresholding detection method used in the Hydrometcentre of Russia [4]. Overall, less than 1% (0.03%) of DCOs had lifetimes exceeding 13 hours, and more than 90% (99.73%) had lifetimes lower than 5 hours, which coincides with the findings of similar studies for the Western Pacific and Australia for the period of November 2009-January 2010 despite the differences in datasets and detection methods [5]. Most DCOs, on average, were detected in May (see Figure 1), which corresponds to the thunderstorm activity peak in Southern Europe. Since severe weather phenomena do not always coincide with detected DCOs, sometimes due to false alarms (some DCOs may be falsely classified as deep convection), DCOs collocated with severe weather (SW) occurrences (DCO-SWs) were selected for further analysis. The number of DCO-SWs has a peak in June, which corresponds to the thunderstorm activity peak in Central and Eastern Europe and may be related to the geographical features of the region, the proximity of the warm Atlantic waters, the greater number of synoptic stations where severe weather is observed and severe weather reports submitted by the citizens (also related to higher population density) [6].

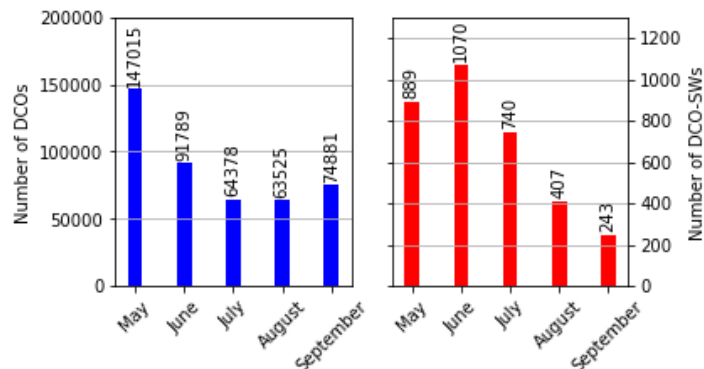


Figure 1. Mean annual number of detected DCOs (left) and DCO-SWs (right)

**Table 1. DCO-SW to DCO ratio for different lifetime and size groups**

Size (sq. km)	Lifetime (hours)				
	< 1	1-6	6-12	12-24	24+
0-25	0.17	0.45	-	-	-
25-80	0.22	0.00	-	-	-
80-310	0.37	1.69	-	-	-
310-700	0.70	3.46	0.00	-	-
700-100000	1.58	15.64	51.69	65.77	73.68
100000-200000	20.0	71.43	87.50	92.03	86.21
> 200000	-	66.67	88.89	93.94	88.24

The study of the DCO-SWs to DCO ratios has revealed that severe weather is observed in 0.05% of cases. The high temporal and spatial variability of DCOs precludes reliable frequency estimation. Thus, approximately 95% of DCOs either did not produce severe weather phenomena or were false alarms. It is also possible that corresponding severe weather phenomena did occur, but were not reported. Statistics from Table 1 suggest that severe weather is most likely to be observed near long-lived large-size DCOs. Probably, most of such DCOs fall into the category of mesoscale convective systems or mesoscale convective complexes, which are associated with the highest risk of severe weather. At the same time, DCOs with lifetimes less than 1 hour are collocated with severe weather phenomena in less than 0.45% of cases (0.17-0.45%, depending on size), which suggests that most of the DCOs are either false alarms or too weak to produce severe weather [7]. However, the lack of severe weather cases can also be explained by the incompleteness of ESWD and SYNOP data.

The results of this study confirm that DCO detection algorithms based on thresholding methods alone are far from perfect. Strong correlation of severe weather occurrences with lifetime and size of a DCO implies that additional criteria involving these parameters can significantly improve the detection skill of such algorithms. Since the process of picking the most effective set of criteria is difficult and labour-intensive, it should be automated using machine learning algorithms.

## References

1. Zinner T., Forster C. of the Meteosat storm detection and nowcasting system Cb-TRAM with lightning network data - Europe and South Africa // Atmospheric Measurement Techniques. – 2013. – Vol. 6. – P. 1567-1583.
2. Silva Neto C.P. da, Barbosa H.A. A method for convective storm detection using satellite data // Atmosfera. – 2016. – Vol. 29. – No 4. – P. 343-358.
3. Dotzek N., P.Groenemeijer, B. Feuerstein, and A.M.Holzer. Overview of ESSL's severe convective storms research using the European Severe Weather Database ESWD // Atmos. Res. – 2009. – No. 93. – P. 575–586.
4. Shishov A., Gorlach I. An Algorithm for the Detection and Tracking of Deep Convection Using Satellite Data and Integer Programming // Proceedings of the Hydrometeorological Research Center of the Russian Federation. – 2020. – Vol. 376. – No 2. – P. 39-59.
5. Hagos S., Feng Z. Environment and the Lifetime of Tropical Deep Convection in a Cloud-Permitting Regional Model Simulation // Journal of the Atmospheric Sciences. – 2013. – Vol. 70. – No 8. – P. 2409-2425.
6. Taszarek M., Allen J. A Climatology of Thunderstorms across Europe from a Synthesis of Multiple Data Sources // Journal of Climate – 2019. – Vol. 32. – P. 1813-1837.
7. Wilson J., Roberts R. Summary of Convective Storm Initiation and Evolution during IHOP: Observational and Modeling Perspective // Monthly Weather Review. – 2006. – Vol. 134. – P. 23-47.